

## Original papers

## A multispectral machine vision system for invertebrate detection on green leaves

Huajian Liu<sup>a,\*</sup>, Javaan Singh Chahl<sup>a,b</sup><sup>a</sup> School of Engineering, University of South Australia, SA, Australia<sup>b</sup> Joint Operations and Analysis Division, Defence Science and Technology Organisation, Canberra, Australia

## ARTICLE INFO

## Keywords:

Machine vision  
Computer vision  
Multispectral imaging  
3D vision  
Invertebrate detection  
Insect detection  
Integrated pest management  
Precision agriculture

## ABSTRACT

Detection and identification of invertebrate pests in farming fields is a prerequisite necessity for integrated pest management (IPM), however, current sensing technologies do not meet the requirements for IPM. Currently, farmers have to first sample pests and then manually count and identify them, in a way that is time-consuming, labour-intensive and error-prone. Machine vision technology has taken over part of the work in a more efficient and accurate manner. However, current machine vision systems (MVSs) have limitations in detecting pests on crops and the counting and identification are constrained in laboratories or pest traps, resulting in the exact time and locations of pests being unknown, hindering more proper decisions and efficient actions. In this study, we developed a multispectral MVS to detect common invertebrate pests on green leaves in natural environment. First, it was found that, besides visible light and near-infrared, the ultraviolet is a good indicator to distinguish green leaves from other materials. Then for multispectral or hyperspectral data processing, we proposed two models, one named normalised hypercube and another named hyper-hue, which are less affected by uneven illumination and can reflect data distribution, resulting in more accurate classification than the normal method of spectral angle mapper (SAM). Further, the relationship between spectral angle and the relative angle of hyper-hue was studied and it was found that usually, data of hyper-hue has larger inter-class distances which could contribute to better classification. At last, to solve the practical problems of image registration and real-time infield applications, instead of registering 2D images, the MVS created and registered 3D point clouds. In an experiment of detecting twelve types of common invertebrate pests on crops, the proposed MVS showed acceptable accuracy.

## 1. Introduction

## 1.1. Research background and aim

Using broad-spectrum pesticide to control invertebrate pests has caused serious problems, including the increase of pesticide resistance, compromise of food safety and the elimination of beneficial species (Clarry, 2013; GRDC, 2012; Umina et al., 2012; Schellhorn et al., 2013). These increasing challenges have driven the implementation of integrated pest management (IPM) which uses the combination of different pest control methods to control pests more efficiently and effectively (Kogan and Hilton, 2009; Boissarda et al., 2008). Detection and identification of invertebrates in farming fields is a prerequisite necessity of IPM because (1) the technique could provide an accurate time when pests occur; (2) it could provide the exact location where crops are infested; (3) based on the time, location and species, a robotic system could take actions in real-time, such as selective spraying, (4)

the information could be forwarded to an IPM system to make more optimised decisions (Liu et al., 2016).

However, current sensing technologies do not meet these requirements. Currently, farmers have to use sweep nets, traps or beat sheets to sample pests in fields, and then manually count and identify the pests (GRDC, 2014). These manual approaches are time-consuming; labour-intensive, error-prone and cannot provide the exact time and location that pests occur. There two research branches for automatic pest detection: acoustic methods and machine vision systems (MVSs). Acoustic methods are suitable for detecting pests in plant tissue, soil or stored grain. While MVSs have provided more efficient and accurate solutions for some counting or identification tasks (Liu et al., 2016). Nevertheless, because of the challenges in natural farming environments, such as unstable sunlight or complex background, most of the studies of MVSs have not focused on detecting pests on plants in natural environment and the current approaches are limited to counting and identifying specimens in sample containers or pest traps. Usually, moths

\* Corresponding author.

E-mail address: [huajian.liu@mymail.unisa.edu.au](mailto:huajian.liu@mymail.unisa.edu.au) (H. Liu).

are trapped or manually caught and then put in an ideal artificial environment for counting and identification (Liu et al., 2016). However, using the approach of “sample and then count”, decisions will tend to be late with reduced effect. Due to their short life cycle, pests might have finished reproduction and the population could have exceeded the threshold for minimal intervention management before adults are detected (Miles, 2015; Baker and Jennings, 2015). Regarding invertebrate pest detection or plant recognition, the visible light and near-infrared (NIR) between 400 and 1500 nm (Singh et al., 2010; Saranwong et al., 2011; Haff et al., 2013; Liu et al., 2014; Liu et al., 2013) and the soft X-ray between 0.1 nm and 10 nm (Chelladurai et al., 2014; Neethirajan et al., 2007; Karunakaran, 2005) have been studied. However, there is very limited literature regarding the ultraviolet (UV) between 300 nm and 400 nm.

Our aim is to develop a robotic system that can detect common pests on crops as early as possible. Pest sensing is a prerequisite, however, it is a research gap. Thus, at the current stage, the specific objective is to develop a vision system that can detect common invertebrate pests on crops in natural farming environments. The system should be more robust to handle the complex conditions in cropping fields and be more accurate for detecting camouflaged pests. Considering the balance between the robustness of detection and feasibility for infield applications, a multispectral imaging system is more effective than a colour camera and more flexible than a hyperspectral imaging system (Liu et al., 2016). As the variety of crops are huge, at the initial stage, to simplify the problems, this study is focusing on to detect pests on green leaves only. First, the spectral features of green leaves in the UV band was studied. Then, two algorithms were designed based on the study of different models, the data distributions of green leaves and the intrinsic relationship between spectral angle and relative angle of hyper-hue. In addition, the conflict between synchronising the time of image acquisition and registering multispectral images was solved using multispectral 3D point cloud registration. Finally, the system was evaluated using twelve types of common invertebrate pests in South Australia.

## 1.2. Preliminaries

This section introduces the preliminaries of hypercube and hyper-hue which are needed in the materials and methods in Section 2.

A set of original hyperspectral or multispectral data is represented in a multi-dimensional space in the form of hypercube. In a hypercube, the direction of a vector represents a certain material while its norm stands for intensity. In the hypercube, the same materials could have different values under different illumination. Hence, the data in a hypercube cannot be directly used for material classification under unstable illumination, such as natural sunlight. One often used method to measure material similarity in a hypercube is the spectral angle, or usually called spectral angle mapper (SAM). SAM can determine the spectral similarity between two spectra by treating them as vectors in a space with dimensionality equal to the number of bands and calculating the angle between the spectra. Smaller angles represent closer matches of the two spectra. As SAM is irrelative to the norms of the vectors, it is less affected by illumination (Kruse et al., 1993; Petropoulos et al., 2010). Although this method is relatively insensitive to illumination, it does not consider the distribution of data, which, from the point of view of probability, should be taken into account for material classification. For example, if the distribution of the data of a certain material is uneven, that is the values of standard deviation are different in different components, then although the points have the same spectral angle to the sample mean, they could have a different probability of being the same material.

Hyper-hue is a high-dimensional analogy to the norm hue transformed from RGB colour space. For material classification in multispectral or hyperspectral data, Liu, et al. (Liu et al., 2017) proposed a high-dimensional colour space named hyper-hue-saturation-intensity (HHSI), which is a high-dimensional analogy to the trichromatic colour

space hue-saturation-intensity (HSI) transformed from the RGB colour cube (Gonzalez and Woods, 1992; Perez and Koch, 1994). In an  $n$ -dimensional hypercube, along with the hyperchromatic axis, which is the segment connecting the points  $(0, 0, \dots, 0)$  and  $(1, 1, \dots, 1)$ , all the points are projected to a space called hyperchromatic space that is perpendicular to the hyperchromatic axis. In this space, the norms of all of the vectors are normalised so that all the points are in the space of a hypersphere with the radius 1. The values of the normalised points in the hypersphere are the values of hyper-hue which is  $(n - 1)$  dimensions. It has been proven that hyper-hue is more robust to uneven illumination when doing material classification (Liu et al., 2017).

## 2. Materials and methods

### 2.1. The spectral features of green leaves at UV band

Considering the balance between the system complexity and the power of detection, the five spectral bands of UV, blue, green, red and NIR were used to detect invertebrates. While for generalisation, the spectral features of green leaves were studied in both multispectral and hyperspectral data. As the spectral features of green leaves from the visible light to near-infrared in the range of 400–1100 nm have been well studied (Shafri et al., 2006; Liu et al., 2013; Liu and Lee, 2015), this section only discusses the spectral features of green leaves in the UV range of 300–400 nm. Liu, et al. (Liu et al., 2016) evaluated the contribution of UV for pest detection through an experiment, however, their study of the spectral features of the UV light is not adequate and need a further investigation. The hyperspectral reflectance data was provided by the floral reflectance database (FReD) (Arnold et al., 2010). A total of 50 sample points of green leaves were randomly selected from over 2000 sample points in the database. The reflectance data is from 300 nm to 699 nm at 1 nm bandwidth, resulting in 400 dimensions for each sample point. The values of the sample points are plotted in Fig. 1, in which each point is plotted with a random colour and the mean and standard deviation of the points are marked with the red and blue bold curve respectively. From the observation, the reflectance of green leaves between the UV bands from 300 nm to 400 nm is below 0.15 which is relatively lower than that at higher spectral bands. In further observation, in the UV bands, the standard deviation is below 0.03, showing that the reflectance of the green leaves is more stable in the UV bands than that at higher spectral bands.

A similar experiment was conducted in a set of multispectral images of UV, blue, green, red and NIR which were collected by a multispectral imaging system developed by Liu, et al. (Liu et al., 2016). The peak transmittance of the filters in the system is 330 nm (UV), 465 nm (blue), 528 nm (green), 630 nm (red) and 748 nm (NIR) respectively. Total 2,960,000 sample points of green leaves were collected from a variety of plants under different illumination and the result is plotted in Fig. 2. It shows that both the mean and standard deviation of the intensity of the UV light is about 0.1 which is lower than those at other bands. In summary, green leaves have relatively lower and more stable reflectance at the UV spectra between 350 and 400 nm. This property of green leaves indicates that UV light would be a good indicator to distinguish green leaves from other materials.

### 2.2. Normalised hypercube

We recommended two models that are less affected by illumination and at the same time can describe the distribution of data: the normalised hypercube (NH) and hyper-hue (Liu et al., 2017). Hyper-hue has been introduced in Section 1.2 and this section explain the concept of NH.

An NH can be simply obtained by normalising the norms of all the vectors in a hypercube to 1. After this transformation, all the points are in a space of hypersphere and each point represents the direction of the corresponding vector in the hypercube and therefore, can represent a

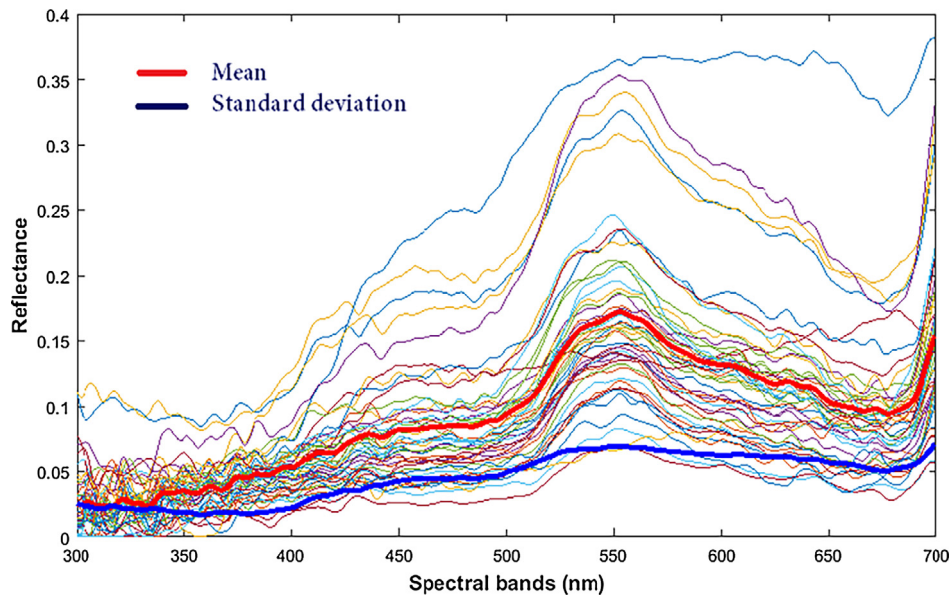


Fig. 1. Reflectance of the sampled green leaves in the FRed database (Arnold et al., 2010).

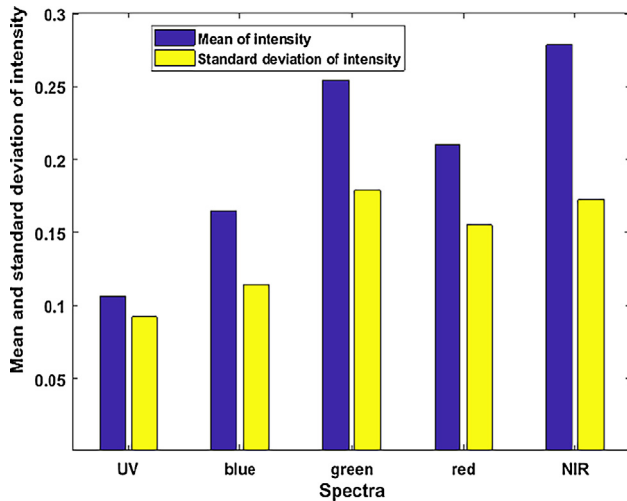


Fig. 2. Mean and standard deviation of the intensity of the sampled green leaves in the multispectral data.

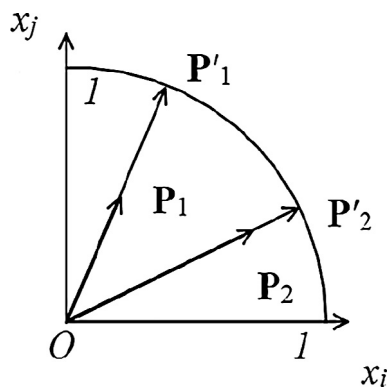


Fig. 3. Normalise hypercube.

certain material. Fig. 3 shows an example of the transformation from a hypercube to an NH.  $x_i$  and  $x_j$  are the two components in a hypercube and  $p_1$  and  $p_2$  are the original data in the hypercube. After normalising the norms of  $p_1$  and  $p_2$  to 1 to obtain  $p'_1$  and  $p'_2$ ,  $p'_1$  and  $p'_2$  are in the

space of NH which is a hypersphere with the radius 1. As the data in a NH represents the directions of the vectors and is irrelative to the norms of the vectors, similar to SAM, the data is less affected by illumination.

### 2.3. Distributions of sample data of green leaves

Understanding the distributions of data in different spaces will aid in developing proper classifiers. In this study, as we focused on distinguishing green leaves from unknown pests, only the distributions of the sample data of green leaves were studied. The hyperspectral and multispectral data introduced in Section 2.1 was used again. The distributions were observed in the principal components (PCs) and some angles related to the PCs. The PCs were obtained using principal component analysis (PCA) and the statistics of sample variance ( $s^2$ ) and percent of variance explained ( $p$ ) in the first four PCs are listed in Table 1. It was found that the distributions of the data were uneven in the PCs. In the hyperspectral and multispectral data, the variance explained in the first PC is 93.72%, and 71.12% respectively. After the fourth PC, the variance explained in each PC is small and can be ignored. The data mainly distributes along the axes of the first three PCs, especially the first one. Three angles were observed and the results are listed in Table 2. The first two angles  $\alpha_1$  and  $\alpha_2$  are the angles between the hyperachromatic axis and the axes of the first and second PCs. The third angle  $\alpha_3$  is the angle between the hyperachromatic axis and the hyperplane spanned by the first and second PCs. In either the hyperspectral or multispectral, the angles are similar and the values of  $\alpha_1$ ,  $\alpha_2$  and  $\alpha_3$  are close to 25°, 81° and 23° respectively. For a better observation, a two-dimensional projection of the hyperspectral data is plotted in Fig. 4, in which the four axes of 300 nm, 500 nm, 700 nm and hyperachromatic axes are marked by the red, green, blue and black colours respectively and the points are plotted as red dots. The axis of

Table 1

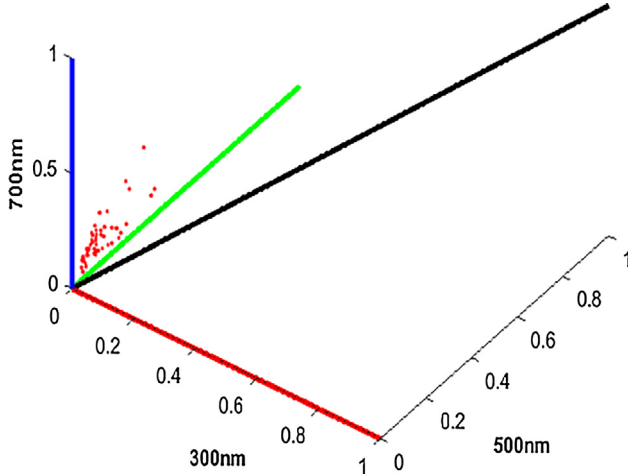
The statistics of the distributions of the sampled green leaves in hypercube.

Hyperspectral data			Multispectral data	
PCs	$s^2$	$p$	$s^2$	$p$
1	0.895	93.72%	0.076	71.12%
2	0.024	2.53%	0.021	19.73%
3	0.020	2.07%	0.008	7.54%
4	0.004	0.46%	0.001	1.23%

**Table 2**

The angles to describe the distributions of the sampled green leaves in hypercube.

	$\alpha_1$	$\alpha_2$	$\alpha_3$
Hyperspectral	24.61°	81.06°	22.72°
Multispectral	25.25°	81.96°	23.77°

**Fig. 4.** A 2D projection of the hyperspectral data of the sampled green leaves.

the first PC starts from the origin of the hypercube, and the angle between it and the hyperachromatic axis is about 25°. It is clear that the distribution of the points is uneven along the axes of the PCs.

The sample data of green leaves was transformed into the spaces of NH and hyper-hue respectively and the statistics of sample variance ( $s^2$ ) and percent of variance explained ( $p$ ) of the first four PCs were calculated and listed in Table 3. Similarly, from the observation of  $p$ , the distributions of the data are uneven along the PCs and most of the variances are in the first two PCs.

#### 2.4. Spectral angle and relative angle of hyper-hue

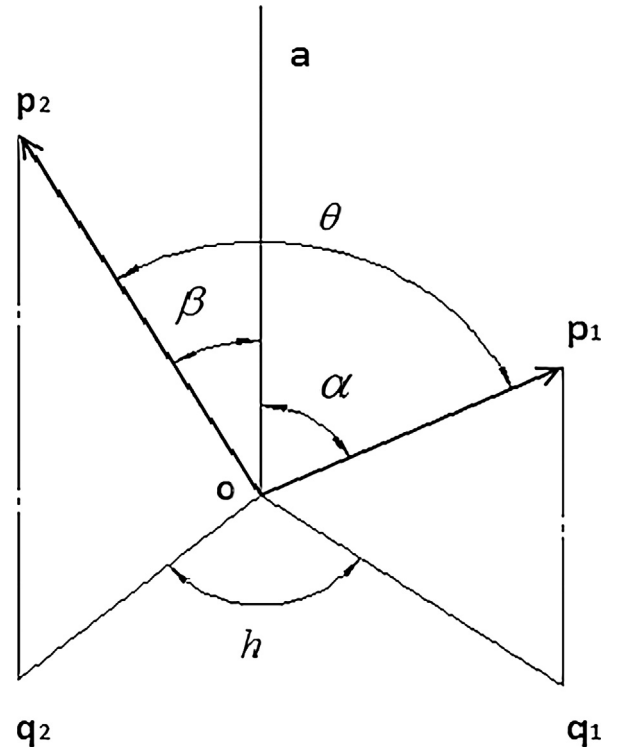
Liu, et al. (Liu et al., 2017) developed the HHSI space but did not explain the intrinsic relationship between spectral angle and relative angle of hyper-hue. However, understanding this relationship will aid in developing proper algorithms and therefore it needs a further discussion. As shown in Fig. 5, suppose the hypercube has the origin  $o$  and hyperachromatic axis  $a$ . There are two vectors  $p_1$  and  $p_2$  in the hypercube. The angle between  $p_1$  and the hyperachromatic axis  $a$  is  $\alpha$ , and the angle between  $p_2$  and  $a$  is  $\beta$ . The spectral angle between  $p_1$  and  $p_2$  is  $\theta$ .  $p_1$  and  $p_2$  are projected along the hyperachromatic axis  $a$  to the hyperchromatic space to obtain the two points  $q_1$  and  $q_2$ . If the norms of  $q_1$  and  $q_2$  are 1, then they can be presented as  $q_1 = (0, h_1)$ ,  $q_2 = (0, h_2)$ , where  $h_1$  and  $h_2$  are hyper-hue of  $p_1$  and  $p_2$  respectively. The

**Table 3**

The statistics of the distributions of the sampled green leaves in the spaces of NH and hyper-hue.

Hyperspectral data					Multispectral data			
PC	$s_n^2$	$p_n$	$s_h^2$	$p_h$	$s_n^2$	$p_n$	$s_h^2$	$p_h$
1	0.006	37.65%	0.025	40.92%	0.063	63.01%	0.355	67.34%
2	0.003	22.17%	0.011	17.38%	0.029	29.31%	0.132	25.08%
3	0.002	11.75%	0.009	14.37%	0.005	4.78%	0.031	5.79%
4	0.001	7.97%	0.005	8.87%	0.002	1.80%	0.009	1.80%

$s_n^2$  stands for the sample variance in NH.  $p_n$  stands for the percent of variance explained in NH. Similarly,  $s_h^2$  and  $p_h$  are for hyper-hue.

**Fig. 5.** Relationship between spectral angle  $\theta$  and relative angle of hyper-hue  $h$ .

relative angle between  $q_1$  and  $q_2$ , or  $h_1$  and  $h_2$ , is  $h$ , the projection of the spectral angle  $\theta$  in the hyperchromatic space. The relation between  $h$ ,  $\alpha$ ,  $\beta$  and  $\theta$  can be found through the following deviation.

From Fig. 5,  $p_1$  and  $p_2$  can be presented as Eqs. (1) and (2) and the norms of them are expressed as Eqs. (3) and (4).

$$p_1 = (1/\tan \alpha, h_1) \quad (1)$$

$$p_2 = (1/\tan \beta, h_2) \quad (2)$$

$$\|p_1\| = 1/\sin \alpha \quad (3)$$

$$\|p_2\| = 1/\sin \beta \quad (4)$$

The dot product of  $q_1$  and  $q_2$  is the same as the dot product of  $h_1$  and  $h_2$ , and it has

$$q_1 \cdot q_2 = h_1 \cdot h_2 = \|h_1\| \|h_2\| \cos h = \cos h. \quad (5)$$

From Eqs. (1), (2) and (5), the dot product of  $p_1$  and  $p_2$  is

$$\begin{aligned} p_1 \cdot p_2 &= (1/\tan \alpha, h_1) \cdot (1/\tan \beta, h_2) \\ &= 1/\tan \alpha \tan \beta + h_1 \cdot h_2 \\ &= 1/\tan \alpha \tan \beta + \cos h. \end{aligned} \quad (6)$$

From Eqs. (3) and (4), the dot product of  $p_1$  and  $p_2$  can also be expressed as

$$p_1 \cdot p_2 = \|p_1\| \|p_2\| \cos \theta = \cos \theta / \sin \alpha \sin \beta. \quad (7)$$

From Eq. (6) and Eq. (7), it has

$$1/\tan \alpha \tan \beta + \cos h = \cos \theta / \sin \alpha \sin \beta. \quad (8)$$

The angle  $h$  can be expressed as

$$h = \arccos(\cos \theta / \sin \alpha \sin \beta - 1/\tan \alpha \tan \beta). \quad (9)$$

where  $\alpha$ ,  $\beta$ , and  $\theta$  should satisfy

$$\alpha \neq 0, \beta \neq 0, |\alpha - \theta| < \beta < \alpha + \theta$$

From the observation of Eq. (9), the relative angle of hyper-hue  $h$  is dependent upon  $\alpha$  and  $\beta$  which determine the position of the spectral



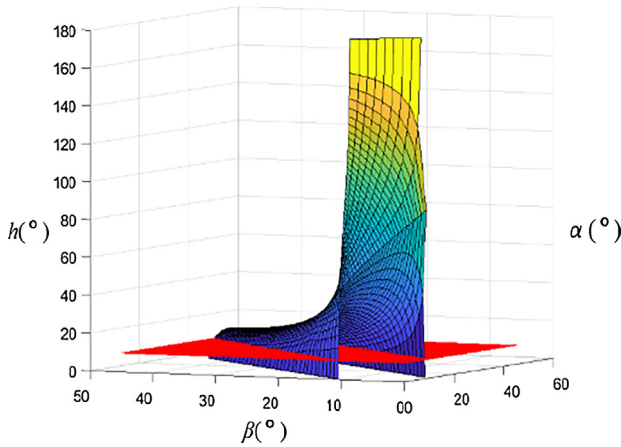


Fig. 6. The values of  $h$  when the spectral  $\theta$  is  $10^\circ$ .

angle  $\theta$ . For better observation, the values of  $h$  were calculated when a spectral angle  $\theta = 10^\circ$  with  $\alpha$  and  $\beta$  were in  $[0^\circ 45^\circ]$  and the results are plotted in Fig. 6. From the observation, when the spectral angle  $\theta$  is projected into the hyperchromatic space to form the relative angle of hyper-hue  $h$ ,  $\theta$  could be either magnified or compressed with different  $\alpha$  and  $\beta$  values. In Fig. 6, the values of  $h$  bigger than  $10^\circ$  are above the red plane and these values are magnified after they are transformed from  $\theta$  to  $h$ . Similarly, those values smaller than  $10^\circ$  are below the red plane and they are compressed. With the different values of  $\alpha$  and  $\beta$ , the possibility of  $h$  being bigger than  $\theta$  is higher. Especially, when the two points  $\mathbf{p}_1$  and  $\mathbf{p}_2$  are very close to the hyperachromatic axis, a smaller spectral angle  $\theta$  can be transformed to a relative angle of hyper-hue up to  $180^\circ$ . With  $\mathbf{p}_1$  and  $\mathbf{p}_2$  moving away from the hyperachromatic axis, the rate of magnification is becoming smaller and stable. The possibility of  $h$  being smaller than the spectral angle  $\theta$  is lower and this case only happens when  $\mathbf{p}_1$ ,  $\mathbf{p}_2$  and the hyperachromatic axis  $\mathbf{a}$  are in the same hyperplane or they are very close to a hyperplane including  $\mathbf{a}$ . In conclusion, when a spectral angle of two points in a hypercube is projected into a hyperchromatic space to form a relative angle of hyper-hue, the angle usually becomes larger. The closer the points are to a hyperachromatic axis, the higher the rate of magnification is. When the points are very close the hyperachromatic axis, the rate of magnification tends to infinity.

The properties of angles in the space of NH and hyper-hue directly affect the intra-class variance and inter-class distances of the data in these spaces. The intra-class variance of the sampled green leaves was measured by standard deviation in the first four PCs. In the hyperspectral data, the average standard deviation in the spaces of NH and hyper-hue is  $s_n = 0.052$  and  $s_h = 0.107$  respectively and the ratio is  $s_h/s_n = 2.087$ . In the multispectral data, the values are 0.133, 0.308 and 2.330 respectively. To measure inter-class distances, twelve common invertebrate pests were imaged using the multispectral imaging system introduced in Section 2.2 and each species was sampled at 1000 points. The inter-class distances are the distances between the sample mean of pests to the sample mean of green leaves. In NH, the average inter-class distance is  $d_n = 0.225$  and in the space of hyper-hue, the distance is  $d_h = 0.557$ . The ratio is  $d_h/d_n = 2.433$ , which is larger than 2.330, the intra-class variance of the multispectral data of the green leaves. Thus, in the space of hyper-hue, the average inter-class distance is relatively longer. When doing classification, it would be ideal to transform original data into a space which has smaller intra-class variance and longer inter-class distance. Hence, from this point of view, hyper-hue may be preferable to NH for material classification.

## 2.5. Classification algorithms

Two algorithms were designed to classify green leaves from other

materials; one used NH and the other used hyper-hue. We have an assumption that the data of hyper-hue and NH has multivariate Gaussian distributions. In essence, for each point, the algorithms calculate the probability of being leaves. For a point, if the probability is higher, it is classified as leaf; otherwise, it is classified as non-leaf. The algorithms can be used for either hyperspectral or multispectral data.

For the first algorithm, the sample data of green leaves was first transformed into the space of NH. The principal axes of the normalised data were found using PCA and then the data was transformed to the coordinate system of the PCs. As the variance mainly exists in the first four PCs, only the data in the first four PCs were used and the sample mean  $\mu_n$  and covariance matrix  $\Sigma_n$  were calculated. A point  $\mathbf{n}$  can be transformed into a semantic value  $s_n$  by

$$s_n = (f(\mathbf{n}))^{\gamma_n} = \left( \exp\left(-\frac{1}{2}(\mathbf{n}-\mu_n)^T \Sigma_n^{-1}(\mathbf{n}-\mu_n)\right) \right)^{\gamma_n}, \quad (10)$$

where  $T$  stands for matrix transpose operation.  $f(\mathbf{n})$  is the normalised probability density function of  $\mathbf{n}$  through which the maximum probability of  $\mathbf{n}$  is normalised to 1.  $\gamma_n$  performs a gamma transformation and it controls the contrast of  $s_n$ . The value of  $\gamma_n$  is in  $(0, \infty)$ . If  $\gamma_n < 1$ , it increases the contrast in the smaller values of  $s_n$  while suppressing the contrast in the bigger values, and vice versa. Eq. (10) is the normalised form of the probability density function of  $\mathbf{n}$  in which the maximum probability is normalised to 1. Thus, the transformed semantic values of  $s_n$  are in the range of  $[0, 1]$ . If a value is closer to 1 then it is semantically closer to green leaf; otherwise, it is semantically closer to other materials. A fixed threshold 0.5 was used for binary classification. If a point's  $s_n$  value was bigger than 0.5 then it was classified as green leaf; otherwise, it was classified as other materials. For the algorithm using hyper-hue, it has the same procedure except that the original data in hypercube need to be transformed to hyper-hue. The corresponding equation of the algorithm is

$$s_h = f(\mathbf{h})^{\gamma_h} = \left( \exp\left(-\frac{1}{2}(\mathbf{h}-\mu_h)^T \Sigma_h^{-1}(\mathbf{h}-\mu_h)\right) \right)^{\gamma_h}, \quad (11)$$

where  $\mathbf{h}$  stands for the value of hyper-hue and  $\mu_h$  and  $\Sigma_h$  are the sample mean and covariance matrix of hyper-hue.  $\gamma_h$  plays the role of gamma transformation and  $s_h$  stands for semantic values.

In this study, as the MVS only has five spectral bands, the transformation of data to PC coordinates was ignored and the data was directly input to the algorithms without PCA. In this case,  $\mathbf{n}$  and  $\mu_n$  in Eq. (10) are  $5 \times 1$  vectors and  $\Sigma_n$  is a  $5 \times 5$  symmetrical matrix. Similarly,  $\mathbf{h}$  and  $\mu_h$  in Eq. (11) are  $4 \times 1$  vectors and  $\Sigma_h$  is a  $4 \times 4$  symmetrical matrix.

## 2.6. Multispectral machine vision system

As pests could move from time to time in farming fields, the time of image acquisition should be synchronised for infield applications. Liu, et al. (Liu et al., 2016) used a broadband camera with a filter wheel to collect multispectral images. This is an acceptable solution for collecting images of stationary objects, however, the images have to be captured at five different times, hindering infield applications. Another solution is using multiple sensors to capture images at different spectral bands simultaneously. Nevertheless, the captured images are in different coordinate systems and must be registered to the same coordinate system for classification algorithms. Although there are many multispectral image registration method available (Pluim et al., 2003; Hasan and Jia, 2012; Fan, 2011; Lee et al., 2009), all of them have the assumption that either the multiple sensors have the same optical centre and only relative rotations around the centre exist or the objects for observation are planar. However, none of the assumptions can be justified in this study.

The conflict has been solved in our previous work of Liu, et al. (Liu et al., 2017). A multispectral MVS has been developed to capture

**Table 4**  
Hardware of the multispectral 3D vision system.

No.	Hardware	Model No.& country	Description
1	UV Camera	CM-140GE-UV, JAI, Yokohama, Japan	GigE Progressive Scan, Sony ICX407BLA sensor, 1/2" CCD, 1392 × 1040 pixels, 31 fps
2	Lens of UV camera	GMUV42528C, Goyo, SAITAMA, Japan	Goyo f25 mm, F2.8, UV Quartz lens, bandpass 200–1200 nm, 30° × 22° × 37°
3	Filter of UV camera	U-340, HOYO, Tokyo, Japan	UV, peak 330 nm, FWHM 85 nm
4	Colour and NIR camera	AD-130GE, JAI, Yokohama, Japan	1/3" progressive scan CCDs, Bayer mosaic colour CCD, monochrome NIR CCD, 1296 (h) × 966 (v), 31 fps
5	Lens of colour and NIR camera	1214, Pentax, Tokyo, Japan	12.5 mm, F1.4; 28.9° × 21.9° × 35.7°

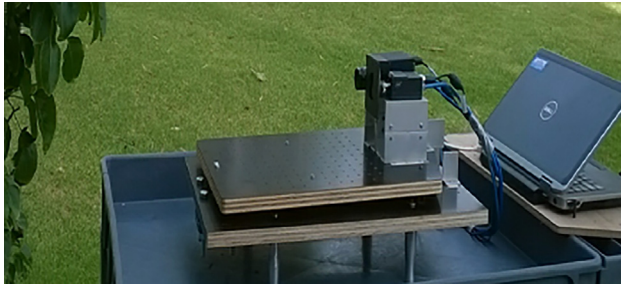


**Fig. 7.** Prototype of the multispectral 3D MVS.

images from two sensors and create 3D point clouds. Instead of registering two-dimensional images, the MVS register point clouds in 3D space, at the same time, the time of image acquisition can be synchronised. For the details of the system, readers are referred to the original paper (Liu et al., 2017), however, for consistency, the system is briefly introduced. Two cameras were used to capture multispectral images simultaneously. The camera AD-130GE (JAI, Yokohama, Japan) was used to capture colour and NIR images and the camera CM-140 (JAI, Yokohama, Japan) was for UV images. Table 4 lists the hardware and specifications of the system. First of all, the cameras were calibrated to obtain the intrinsic and extrinsic parameters for 3D reconstruction and alignment of camera coordinate systems. The workflow includes five steps: (1) The system captured UV, NIR and colour images from two points of view. (2) The colour images were decomposed to red, green and blue images and therefore each dataset included five pairs of images. (3) A 3D point cloud was reconstructed in each spectral band, resulting in five point clouds. (4) The point clouds were registered to the same coordinate system. (5) The intensity values of the multispectral images were mapped to the corresponding 3D points. Fig. 7 shows the prototype of the MVS. Note that, at this stage, in step (1), the two cameras need to be rotated together to capture images from two points of view. However, in a final product, two sets of the same cameras will be used to capture images simultaneously.

## 2.7. Experiments

### 2.7.1. Data collection

A total of twelve types of common invertebrate pests in South Australia were used to test the system and algorithms and the names of the pests are listed in Table 5. A total of 1668 sets of data were collected in different cropping fields and gardens during daytime using the natural sunlight or at night using an artificial illumination. 30 sets of data for each species were randomly selected for testing.

### 2.7.2. Error evaluation

To evaluate the performance of detection, the automatic classification results need to be compared with ground-truth classifications. However, the ground-truth information of the plants and pests are difficult to measure in a 3D world. A trade-off solution is to measure the errors in 2D images, in which, accurate classification can be achieved manually. In a cloud, the points detected as pest can be back-projected to the corresponding 2D images. In the 2D images, these points are

**Table 5**  
Invertebrates studied in the experiment.

	Common name	Scientific name
1	Brown Garden snail (BGS)	<i>Cornu aspersum</i>
2	Vineyard snail (VS)	<i>Cerutuella virgate</i>
3	White garden snails (WGS)	<i>Theba pisana</i>
4	Greenhouse slug (GS)	<i>Milax gagates</i>
5	Australian plague locusts (APL)	<i>Chortoicetes terminifera</i>
6	Brown coloured larva of Looper moth (LLM)	Geometridae
7	Portuguese millipede (PM)	<i>Ommatolius moreleti</i>
8	Earwig (E)	Dermaptera
9	Vegetable grasshopper (VG)	<i>Atractomorpha</i>
10	Larva of orange-striped oakworm (LOO)	<i>Anisota senatoria</i>
11	Larva of diamondback moth (LDM)	<i>Plutella xylostella</i>
12	Larva of green fruit worm (LFW)	<i>Lithophane antennata</i>

sparse and do not have clear boundaries. An image dilation operation with a square structure of 15 pixels was performed to connect these points, resulting in several continuous regions. Fig. 8(a) shows an example of an automatic classification result of a garden snail and Fig. 8(b) shows the corresponding manual classification.

The types of errors defined in statistical hypothesis testing were used. In Fig. 9, if the blue full lines represent manual segmentation and the black-white dot lines represent automatic segmentation, then the image is separated into four parts: true positive (TP), true negative (TN), false positive (FP) and false negative (FN). If  $e_I$  and  $e_{II}$  denote Type I (or false positive rate) and Type II (or false negative rate) error respectively, then Type I errors have the form of

$$e_I = \frac{FP}{FP + TN} 100\%, \quad (12)$$

and Type II errors have the form of

$$e_{II} = \frac{FN}{FN + TP} 100\% \quad (13)$$

### 2.7.3. Experimental results

The developed NH and hyper-hue algorithms were compared with the often-used method SAM. It is ideal to keep both types of errors at lower levels, however, it is hard to achieve in practice. According to different applications and requirements, users should select thresholds that form a compromise between Type I and Type II errors. In this experiment, we tried to keep the Type II errors under 20%, while, the Type I errors were not constrained. By adjusting the gamma values of the hyper-hue and NH algorithms and the threshold of SAM, the type II errors can be controlled to the same level approximately and therefore their accuracy of detection can be compared using the Type I errors only. Fig. 10 shows the examples of point clouds and classification results of the hyper-hue algorithm for the larvae of looper moths, earwigs, larvae of orange-striped oakworms and green fruit worms respectively. The errors of detection are summarised in Figs. 11 and 12.

When the Type II errors are similar, in each of the species, the SAM algorithm has a higher Type I error than the NH and hyper-hue algorithm. In average, the Type I errors are 24.07%, 12.29% and 7.83% for the SAM, NH and hyper-hue algorithm respectively.

The specimens can be separated into two groups according to the

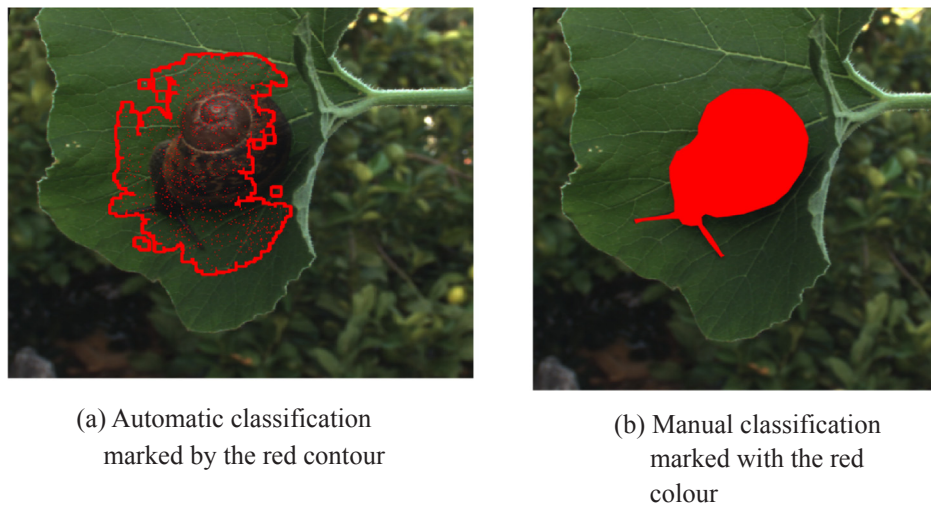


Fig. 8. Example images for evaluating the errors.

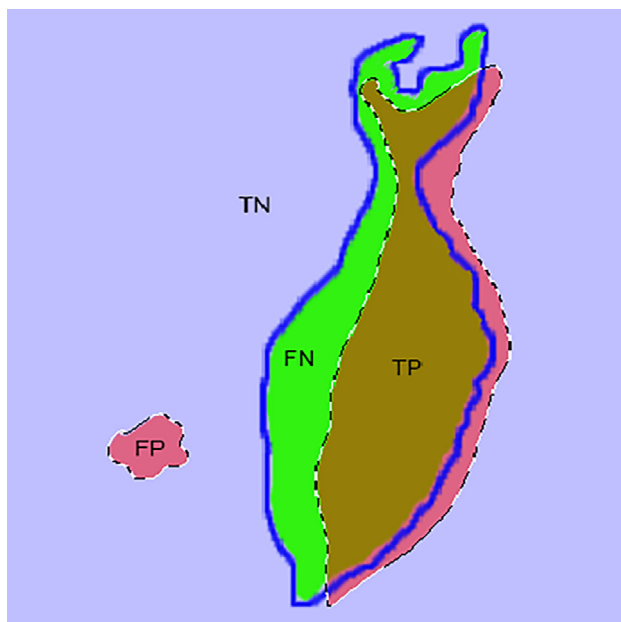


Fig. 9. Definition of type errors.

levels of difficulty in detection: non-camouflaged pests and camouflaged pests. The camouflaged specimens include vegetable grasshoppers, larvae of orangestriped oakworm, larvae of diamondback moth and larvae of green fruit worm. Generally speaking, the non-camouflaged specimens have distinctive spectral features to green leaves and therefore have lower errors. For the NH and hyper algorithms, the Type II errors can be controlled to the level between 10% and 20%, at the same time, the Type I errors are below 20%. While compared with the NH algorithm, the hyper-hue algorithm has lower or similar Type I errors, indicating that it has a higher accuracy for detecting non-camouflaged pests.

In detecting the camouflaged specimens, using either the algorithm of Hyper-hue or NH, the Type II errors cannot be further reduced below a certain level, regardless of adjustments of the gamma values. For example, when using the hyper-hue algorithm to detect the vegetable grasshoppers, by increasing the gamma value to 2.5, the Type II error was reduced to 35.70%. However, when the gamma value was increased further, the error did not change further. For the camouflaged specimens, Type II errors were controlled between 30% and 50% and Type I errors were kept below 20%. The method using hyper-hue did

not show a clear advantage over the method using NH in detecting the camouflaged pests. Only some organs of the camouflaged pests, such as heads or wings, have different spectral features from green leaves and can be detected. However, even in the multispectral image, some parts of their bodies have the similar spectral feature to green leaves and therefore the Type II errors cannot be further reduced when they reach to certain levels.

In summary, the machine vision system could detect the existence of the twelve invertebrates on green leaves using the three algorithms. In each species, the developed NH and hyper-hue algorithms have lower errors than the SAM. For the non-camouflaged specimens, both the NH and hyper-hue algorithms have lower errors, while the hyper-hue algorithm has a higher accuracy than the NH algorithm. In the camouflaged specimens, both the hyper-hue and NH algorithms have relatively higher Type II errors with acceptable Type I errors. The hyper-hue algorithm does not have a clear advantage in detecting the camouflaged pests. On average, the hyper-hue algorithm has the highest accuracy, followed by the NH and SAM algorithms.

### 3. Discussion

The colour, NIR and UV spectra play different roles in the detection. For the non-camouflaged specimens, such as Australian plague locusts and brown garden snails, usually, the colour images can provide enough spectral information for correct detection, however, NIR and UV images could improve the accuracy of detection. For some of the camouflaged specimens, the contributions of UV are significant. For example, the differences between the vegetable grasshoppers and green leaves are not clear in the colour and NIR images while their wings and joints reflect UV light. For the larvae of orangestriped oakworms, their heads and strips on their bodies reflect a small amount of UV light while most parts of their bodies absorb NIR light, resulting in more distinctive features. Fig. 13 shows an example of a green fruit worm. In the colour and NIR images, the worm has the similar spectral features to the plant. While in the UV image, because the plant absorbed most of the UV light and the worm deflected most of it, the worm became distinctive.

For material classification in hyperspectral or multispectral images, the usual method is SAM. One of the main contributions of this study is that we have developed the models of NH and HH which could optimise original high-dimensional data and therefore, can provide more options to develop more elegant methods. In this study, using the model of NH and hyper-hue, we developed the algorithms that can estimate the probability of being leaf or pest for every point and compared them with the method using SAM. Because the NH and hyper-hue algorithms consider the distributions of data, they have better classification



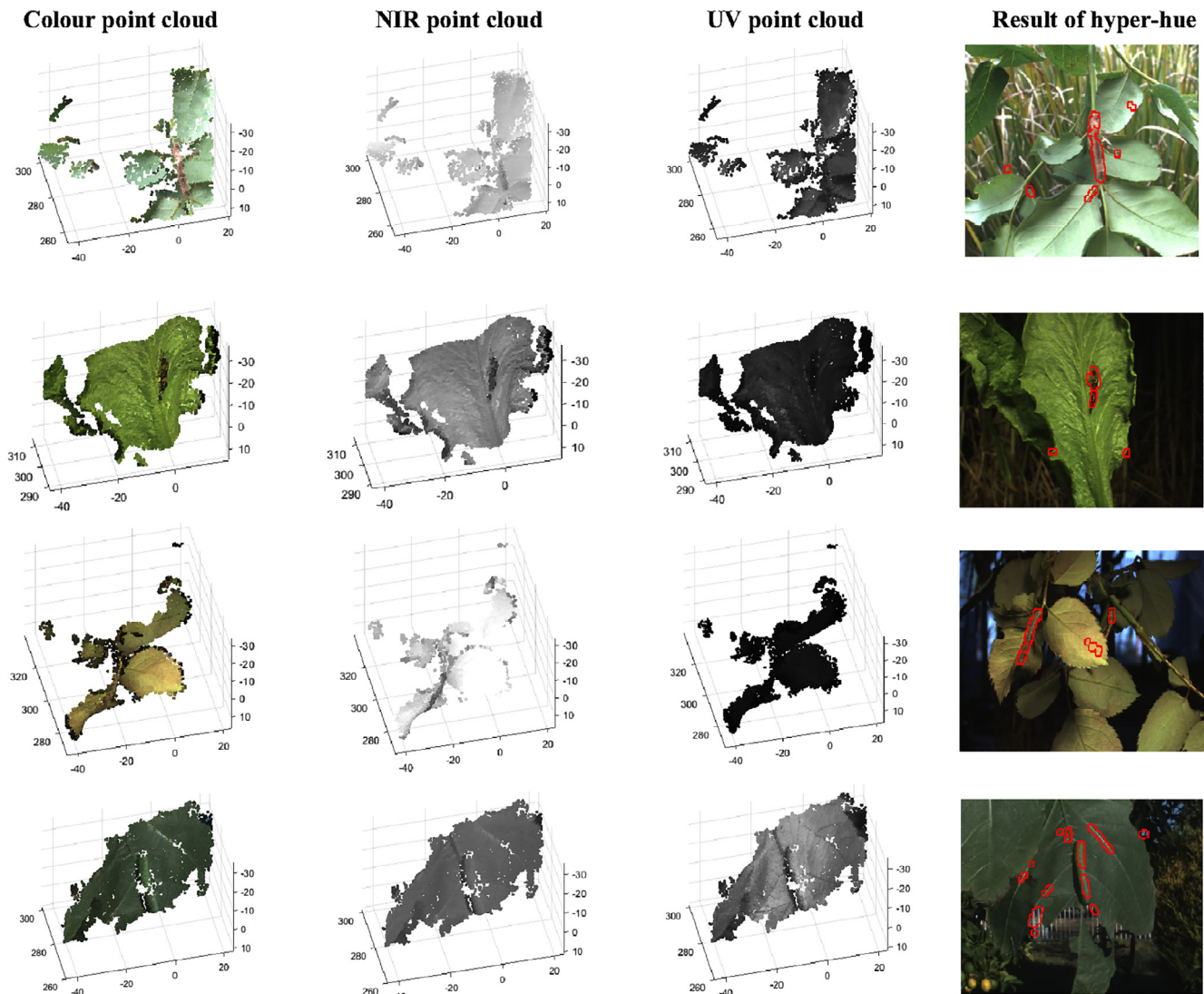


Fig. 10. Example images in the experiment.

accuracy than SAM. Further, the hyper-hue algorithm is better than the NH algorithm because it usually enlarges inter-class distance. From the observation of the data in Section 2.3, hyper-hue space has both longer inter-class distances and larger intra-class variance than NH. In the experimental results of the non-camouflaged specimens, the spectral information was relatively reliable; thus, in the space of hyper-hue, the beneficial effect of larger inter-class distances played more roles than the harmful effect of larger intra-class variance, resulting in more

accurate detection. For the camouflaged specimens, the spectral information was not distinctive and therefore, the advantage of hyper-hue was not clear. In this study, we focused on developing new models to optimise high-dimensional data; thus, the algorithms were designed as simple as possible. In fact, there are many more sophisticated algorithms available for material classification in hyperspectral or multispectral data, such as support vector machine (SVM) (Moughal, 2013; Kavitha et al., 2015) or artificial neural network (ANN) (Patteti et al.,

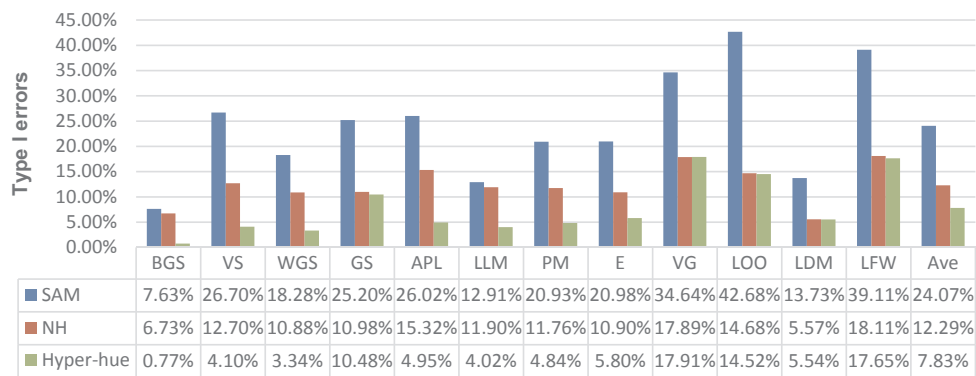


Fig. 11. Type I error (False positive rate).



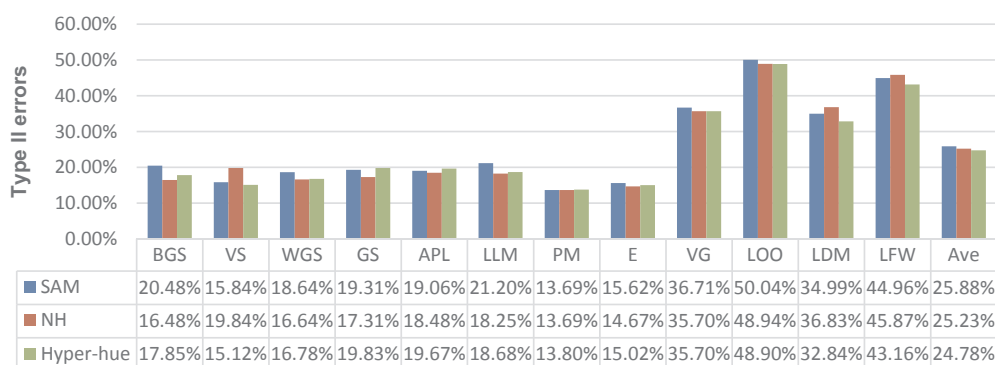


Fig. 12. Type II errors (False negative rate).

2015; Rojas-Moraleda et al., 2017). The interesting thing is how to select suitable models and input data. For example, one could input original data into an ANN for classification and the other might first transform the original data into hyper-hue and then input it into an SVM. This topic is not trivial and worth further investigation.

Instead of processing the 2D images, the reconstruction of 3D models has several advantages. First, the MVS can capture the multi-spectral images from the two sensors at the same time and then create and register the 3D models in 3D space; thus the system is better suited to detecting moving objects. Second, some challenging image segmentation work in 2D images becomes easier in 3D clouds. As in Fig. 10, some materials in the background could have the similar spectral features to the pests or host plants and in principle could not be distinguished in 2D images. However, as these materials were further from the sensors than the pests and the host plant when they were being imaged, they can be separated by the values of depth in 3D point clouds. At last, the 3D point clouds can also provide rich 3D morphological information of plants and invertebrates which are very valuable for pest detection. An initial study of using 3D point clouds to detect invertebrate pests has been conducted by Liu, et al. (Liu et al., 2017). The drawback of using 3D point clouds is that if objects lack rich features, then the created point clouds could be incomplete or include noises because of the correspondence errors of feature points. However, usually, there are rich features in the images of plants or pests and hence, this is not a critical problem for pest detection.

The computational speed of the algorithms was tested in Matlab 2016b on a laptop computer with Intel 2.6 GHz CUP and 8 GB RAM. Depending on the number of points in a point clouds, the average processing time is 0.11–0.15 s and 0.11–0.19 s for the NH and hyper-hue algorithm respectively.

In the future work, the proposed MVS could be used as a sensor for automatic pest detection in two different ways, pest mapping or real-time detection. In the first approach, the system could be mounted on a platform, such as UAV, to collect data faster, followed by off-line processing to generate pest maps which can aid an IPM system to make

optimised pest control plans. In another way, the system could be integrated into an automatic pesticide spray system for real-time pest detection and selective spray.

#### 4. Conclusion

Aiming at detecting common invertebrate pests on crops in natural farming fields, a multispectral 3D MVS was developed. The contributions of this study include: (1) It was found that UV light has relatively lower and more stable reflectance on green leaves and is a good indicator to distinguish green leaves from other materials. (2) We proposed two models, NH and hyper-hue which can optimise original high-dimensional data and provide more options for developing different classification methods. (3) The distributions of the sample data of green leaves were studied in different colour spaces and the uneven distributions should be considered when doing classification. (4) The relationship between spectral angle and the relative angle of hyper-hue was studied. When a spectral angle is projected to a relative angle of hyper-hue, the angle is usually enlarged, resulting in larger inter-class distances which would be beneficial for classification. (5) Two classification algorithms were designed using the proposed model of NH and hyper-hue respectively and they are more accurate than SAM. While the hyper-hue algorithm showed the best classification result. (6) The conflict between multispectral image registration and synchronisation of image acquisition was solved by creating and registering 3D point clouds. In the experiment of using twelve types of specimens including common camouflaged or non-camouflaged pests, the system showed acceptable errors for detecting pests in natural farming environments. The MVS could be used as a sensor for pest mapping or on-the-go pesticide spraying.

#### Acknowledgements

Some of the equipment for this project was borrowed from Project Tyche, the trusted autonomy initiative of the Defence Science and

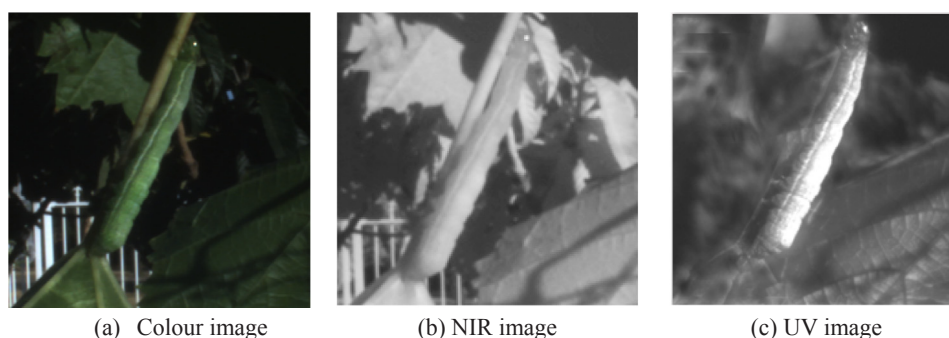


Fig. 13. The example images show the contribution of UV.

Technology Group, Australian Department of Defence.

## References

- Clarry, S., Insecticide Resistance Increasing in Aphids. Available: <http://www.grdc.com.au/Media-Centre/Ground-Cover/Ground-Cover-Issue-106-Sept-Oct-2013/Insecticide-resistance-increasing-in-aphids>, 2013, (Last accessed 10 May, 2016).
- GRDC, Insecticide Resistance Management and Invertebrate Pest Identification Fact Sheet. Available: <http://rawbrown.com.au/pdf/agribusiness/Fact-Sheet-1.pdf>, 2012, (Last accessed 9 Sep, 2015).
- Umina, P.A., Weeks, A.R., Roberts, J., Jenkins, S., Mangano, G.P., Lord, A., Micis, S., 2012. The current status of pesticide resistance in Australian populations of the redlegged earth mite (*Halotydeus destructor*). *Pest Manage. Sci.* 68, 889.
- Schellhorn, N., Renwick, A., Macfadyen, S. The Real Cost of Pesticides in Australia's Food Boom. Available: <http://theconversation.com/the-real-cost-of-pesticides-in-australias-food-boom-20757>, 2013, (Last accessed 10 July, 2016).
- Kogan, M., Hilton, R.J. 2009. Conceptual framework for integrated pest management (IPM) of tree-fruit pests. In: *Biorational Tree-Fruit Pest Management*, vol. 1, Oxfordshire, UK: Centre for Agriculture and Biosciences International. <http://doi.org/10.1079/9781845934842.0001>.
- Boissarda, P., Martinb, V., Moisanb, S., 2008. A cognitive vision approach to early pest detection in greenhouse crops. *Comput. Electron. Agric.* 62, 81–93.
- Liu, H., Lee, S.H., Chahl, J.S., 2016. A review of recent sensing technologies to detect invertebrates on crops. *Precision Agric.* 17. <http://dx.doi.org/10.1007/s11119-016-9473-6>.
- GRDC, Slugging Slugs. Available: <http://grdc.com.au/Media-Centre/Hot-Topics/Slugging-slugs>, 2014, (Last accessed 18, July, 2016).
- Miles, M., Insect Pest Management in Faba Beans. Available: <https://grdc.com.au/Media-Centre/Ground-Cover/Ground-Cover-Issue-117-July-August-2015/Insect-pest-management-in-faba-beans>, 2015, (Last accessed 7 Oct, 2015).
- Baker, G., Jennings R. Growers Chase Pest-Control Answers. Available: <https://grdc.com.au/Media-Centre/Ground-Cover/Ground-Cover-Issue-117-July-August-2015/Growers-chase-pest-control-answers>, 2015, (Last accessed 8 Aug., 2016).
- Singh, C., Jayas, D., Paliwal, J., White, N., 2010. Identification of insect-damaged wheat kernels using short-wave near-infrared hyperspectral and digital colour imaging. *Comput. Electron. Agric.* 73, 118–125.
- Saranwong, S., Haff, R., Thanapase, W., Janhira, A., Kasemsumran, S., Kawano, S., 2011. A feasibility study using simplified near infrared imaging to detect fruitfly larvae in intact fruit. *Near Infrared Spectrosc.* 19, 55–60.
- Haff, R., Saranwong, S., Thanapase, W., Janhira, A., Kasemsumran, S., Kawano, S., 2013. Automatic image analysis and spot classification for detection of fruit fly infestation in hyperspectral images of mangoes. *Postharvest Biol. Technol.* 86, 23–28.
- Liu, H., Lee, S.H., Saunders, C., 2014. Development of a machine vision system for weed detection during both off-season and in-season in broadacre no-tillage cropping lands. *Am. J. Agric. Biol. Sci.* 9, 174–193. <http://dx.doi.org/10.3844/ajabssp.2014.174.193>.
- Liu, H., Saunders, C., Lee, S.H., 2013. Development of a proximal machine vision system for off-season weed mapping in broadacre no-tillage fallows. *J. Comput. Sci.* 9, 1803–1821. <http://dx.doi.org/10.3844/jcscsp.2013.1803.1821>.
- Chelladurai, V., Karuppiyah, K., Jayas, D., Fields, P., White, N., 2014. Detection of *Callosobruchus maculatus* infestation in soybean using soft X-ray and NIR hyperspectral imaging techniques. *J. Stored Prod. Res.* 57, 43–48.
- Neethirajan, S., Jayas, D.S., White, N.D.G., 2007. Detection of sprouted wheat kernel using soft X-ray image analysis. *J. Food Eng.* 81, 509–513.
- Karunakaran, C., Paliwal, J., Jayas, D.S., White, N.D.G. 2005. Comparison of Soft X-rays and NIR Spectroscopy to Detect Insect Infestations in Grain. Paper No. 053139, ASAE St. Joseph, MI, USA.
- Kruse, F.A., Lefkoff, A.B., Boardman, J.W., Heidebrecht, K.B., Shapiro, A.T., Barloon, P.J., et al., 1993. The spectral image processing system (SIPS) - interactive visualization and analysis of imaging spectrometer data. *Remote Sensing Environ.* 44, 145–163. [http://dx.doi.org/10.1016/0034-4257\(93\)90013-n](http://dx.doi.org/10.1016/0034-4257(93)90013-n).
- Petropoulos, G.P., Vadrevu, K.P., Xanthopoulos, G., Karantounias, G., Scholze, M., 2010. A comparison of spectral angle mapper and artificial neural network classifiers combined with Landsat TM Imagery analysis for obtaining burnt area mapping. *Sensors* 10, 1967–1985. <http://dx.doi.org/10.3390/s100301967>.
- Liu, H., Lee, S.H., Chahl, J.S., 2017. Transformation of a high-dimensional colour space for material classification. *J. Opt. Soc. Am. A* 34, 523–532. <http://dx.doi.org/10.1364/josaa.34.000523>.
- Gonzalez, R.C., Woods, R.E., 1992. *Digital Image Processing*, Boston, MA. Addison-Wesley Publishing Company Inc, USA.
- Perez, F., Koch, C., 1994. Toward colour image segmentation in analog VLSI: algorithm and hardware. *Int. J. Comput. Vision* 12, 17–42. <http://dx.doi.org/10.1007/BF01420983>.
- Shafri, H., Salleh, M., Ghiyam, A., 2006. Hyperspectral remote sensing of vegetation using red edge position techniques. *Am. J. Appl. Sci.* 3, 1864–1871.
- Liu, H., Li, P., Saunders, C., Lee, S.H. 2013. Development of a green plant image segmentation method of machine vision system for no-tillage fallow weed detection. In: *Society for Engineering in Agriculture Conference : Innovative Agricultural Technologies for a Sustainable Future*, Mandurah, WA, Australia, pp. 95–108.
- Liu, H., Lee, S.H. 2015. Stitching of video sequences for weed mapping. In: *International Conference on Intelligent Information Hiding and Multimedia Signal Processing (IIH-MSP)*, Adelaide, Australia, pp. 441–444. <http://doi.org/10.1109/IIH-MSP.2015.106>.
- Liu, H., Lee, S.H., Chahl, J.S., 2016. An evaluation of the contribution of ultraviolet in fused multispectral images for invertebrate detection on green leaves. *Precision Agric.* 17. <http://dx.doi.org/10.1007/s11119-016-9472-7>.
- Arnold, S., Faruq, S., Savolainen, V., McOwan, P., Chittka, L., 2010. The floral reflectance database—a web portal for analyses of flower colour. *PLoS One* 5. <http://dx.doi.org/10.1371/journal.pone.0014287>.
- Pluim, J.P.W., Maintz, J.B.A., Viergever, M.A., 2003. Mutual-information-based registration of medical images: a survey. *IEEE Trans. Med. Imaging* 22, 986–1004. <http://dx.doi.org/10.1109/TMI.2003.815867>.
- Hasan, M., Jia, X. 2012. *Reliable Multi-Modal Automatic Remote Sensing Image Registration*. PhD Thesis, Engineering & Information Technology, University of New South Wales, Canberra, Australia.
- Fan, X. 2011. *Automatic Registration of Multi-Modal Airborne Imagery*. PhD Thesis, Rochester Institute of Technology, Ann Arbor, United States. ISBN: 9781124663555.
- Lee, D., Hofmann, M., Steinke, F., Altun, Y., Schölkopf, B., Cahill, N.D. 2009. Learning similarity measure for multi-modal 3D image registration. In: *IEEE Computer Society Conference on Computer Vision and Pattern Recognition Workshops*, pp. 186–193. <http://doi.org/10.1109/CVPRW.2009.5206840>.
- Liu, H., Lee, S.H., Chahl, J.S., 2017. Registration of multispectral 3D points for plant inspection. *Precision Agric.* <http://dx.doi.org/10.1007/s11119-017-9536-3>.
- Moughal, T., 2013. Hyperspectral image classification using Support Vector Machine. *J. Phys.: Conf. Series* 439, 1–9. <http://dx.doi.org/10.1088/1742-6596/439/1/012042>.
- Kavitha, K., Arivazhagan, S., Sangeetha, I.K., 2015. Hyperspectral image classification using Support Vector Machine in Ridgelet Domain. *National Acad. Sci. Lett.*, vol. 38, pp. 475–478. <http://doi.org/10.1007/s40009-015-0361-9>.
- Patteti, S., Samanta, B., Chakravarty, D., 2015. Design of a feature-tuned ANN model based on bulk rock-derived mineral spectra for endmember classification of a hyperspectral image from an iron ore deposit. *Int. J. Remote Sensing* 36, 2037–2062. <http://dx.doi.org/10.1080/01431161.2015.1031920>.
- Rojas-Moraleda, R., Valous, N., Gowen, A., Esquerre, C., Härtel, S., Salinas, L., et al., 2017. A frame-based ANN for classification of hyperspectral images: assessment of mechanical damage in mushrooms. *Neural Comput. Appl.* 28, 969–981. <http://dx.doi.org/10.1007/s00521-016-2376-7>.
- Liu, H., Lee, S.H., Chahl, J.S. 2017. A multispectral 3D vision system for invertebrate detection on crops. *IEEE Sensors* pp. 1–14. <http://doi.org/10.1109/JSEN.2017.2757049>.